

Journal of Materials Chemistry A

Accepted Manuscript



This is an *Accepted Manuscript*, which has been through the Royal Society of Chemistry peer review process and has been accepted for publication.

Accepted Manuscripts are published online shortly after acceptance, before technical editing, formatting and proof reading. Using this free service, authors can make their results available to the community, in citable form, before we publish the edited article. We will replace this *Accepted Manuscript* with the edited and formatted *Advance Article* as soon as it is available.

You can find more information about *Accepted Manuscripts* in the [Information for Authors](#).

Please note that technical editing may introduce minor changes to the text and/or graphics, which may alter content. The journal's standard [Terms & Conditions](#) and the [Ethical guidelines](#) still apply. In no event shall the Royal Society of Chemistry be held responsible for any errors or omissions in this *Accepted Manuscript* or any consequences arising from the use of any information it contains.

General strategy of decorating 3D carbon nanofiber aerogel derived from bacterial cellulose with nano-Fe₃O₄ for high-performance flexible and binder-free lithium-ion battery anodes

Yizao Wan ^{a,b}, Zhiwei Yang ^a, Guangyao Xiong ^{b,*}, Honglin Luo ^{a,*}

^a *School of Materials Science and Engineering, Tianjin Key Laboratory of Composite and Functional Materials, Key Laboratory of Advanced Ceramics and Machining Technology, Ministry of Education, Tianjin University, Tianjin 300072, China*

^b *School of Mechanical and Electrical Engineering, East China Jiaotong University, Nanchang 330013, China*

Corresponding authors.

E-mail addresses: xiongguangyao@163.com (G. Xiong), hlluotju@126.com (H. Luo)

Abstract

Flexible, binder-free, and cost-effective materials have been highly sought after in the development of next generation electrodes. Herein, we report the general, scalable, and eco-friendly synthesis of a novel flexible nano-Fe₃O₄-decorated three-dimensional (3D) carbon nanofiber (CNF) aerogel derived from bacterial cellulose (BC) (named as Fe₃O₄-BC-CNFs) via the hydrothermal approach followed by carbonization. The as-prepared Fe₃O₄-BC-CNFs electrodes with optimal Fe₃O₄ loading exhibit greatly improved electrochemical performance over bare BC-CNFs and Fe₃O₄ nanoparticles. Furthermore, compared with most of other relevant types of electrodes, the flexible and binder-free Fe₃O₄-BC-CNFs electrodes can deliver a higher reversible capacity of 754 mAh g⁻¹ (after 100 cycles at 100 mA g⁻¹). The excellent electrochemical performance is ascribed to the highly dispersed Fe₃O₄ nanoparticles on CNFs, the 3D porous structure, large surface area, and the interconnected CNFs, which offer a large material/electrolyte contact area, promote high diffusion rate of Li ions, and accommodate volume changes of the active materials during cycling. The excellent flexibility and high reversible capacity of the electrodes as well as the eco-friendly and scalable process make them promising in the development of flexible energy-storage devices.

Carbon materials have long been used as anode materials in lithium-ion batteries (LIBs) due to their low price, low lithium ion intercalation potential and good cyclic stability.¹ However, conventional carbon anodes have small energy capacity, and the diffusion of the Li ions between carbon layers is not fast enough.¹ Using nano-sized materials to prepare electrodes is one of the most promising routes toward making high-performance batteries.² Thus, researchers worldwide are dedicated to developing carbon nanomaterials as replacements of conventional carbon materials. Up to now, nano-scaled carbonaceous materials such as carbon nanotubes (CNTs), graphenes, and carbon nanofibers (CNFs) have been widely studied as potential electrodes for LIBs.³⁻⁶ Nonetheless, those carbon nanomaterials were generally produced by sophisticated chemical vapor deposition (CVD), or multistep exfoliation and reduction methods. The high-cost synthesis impedes their practical and commercial applications. Apart from graphenes, CNTs, and CNFs prepared by the CVD method, CNFs made from electrospun precursors have also been extensively studied as reviewed by Inagaki and co-workers.⁷ Yu and co-workers have reported a simple route to fabricate CNF aerogels on a large scale,⁸ which has paved a new way for the fabrication of low-cost carbon nanomaterials. The same group⁹ as well as our group¹⁰ have also reported the production of free-standing CNFs from bacterial cellulose (BC) hydrogels. BC is a low-cost, environmentally friendly, and abundant natural polysaccharide synthesized by various nonpathogenic bacteria species such as *Acetobacter xylinum* and has long been produced on industrial scales. More importantly, although the flexibility of graphene and CNTs-based materials mainly

relies on flexible substrates,¹¹⁻¹³ Yu et al. have declared that the BC-derived CNFs (denoted as BC-CNFs hereinafter) are highly conductive and exhibit good flexibility,¹⁴ which makes it possible to prepare flexible electrodes based on BC-CNFs. Previous studies using BC-CNFs¹⁵ and other CNFs such as electrospun CNFs¹⁶⁻¹⁹ have demonstrated good electrochemical performance as anodes for LIBs. It should be pointed out, however, that the energy density delivered by bare CNFs is usually limited by the amount of lithium that can be inserted.²⁰ A general and effective way of improving the capacity of bare CNFs is to load high-performance active materials such as metal oxides onto the CNFs.²¹⁻²⁴

In a pioneering work by Wang and co-workers, SnO₂ nanoparticles were decorated on BC-CNFs by a hydrolyzation process to fabricate a new anode for LIBs.²⁵ Encouraged by their work, we have prepared nano-Fe₃O₄-decorated BC-CNFs (denoted as Fe₃O₄-BC-CNFs hereinafter) for LIB applications. Compared with previous reports, our approach and the resultant materials possess some distinct features. Firstly, unlike previous studies where BC-CNFs were used as the substrates for decoration of SnO₂ nanoparticles and glycol was used as solvent,²⁵ we employed an eco-friendly two-step approach of hydrothermal process and subsequent carbonization. In the first step, organic BC nanofibers were used as the substrate and deionized water was used as the solvent of iron source solution for the immobilization of Fe₂O₃ nanoparticles. The use of BC aerogels rather than BC-CNFs^{25, 26} favors the uniform distribution of Fe₂O₃ nanoparticles since the abundant hydroxyl functional groups on BC nanofibers act as nucleation sites for Fe₂O₃ nanoparticles. The use of deionized

water rather than an organic solvent²⁵ can reduce the environmental impact, making the process eco-friendly. Secondly, iron oxides including Fe₃O₄ and Fe₂O₃ have recently received increased attention as very promising anode materials for LIBs.^{27, 28} Compared with SnO₂, Fe₃O₄ exhibits a higher theoretical capacity (925 vs. 790 mAh g⁻¹). Fe₃O₄ is more abundant, more cost-effective (in terms of the raw materials), and more environmentally benign, making it a more promising electrode material. Additionally, the deposition of Fe₂O₃ nanoparticles can be easily controlled in terms of coating thickness. Lastly and more importantly, the binder-free and free-standing Fe₃O₄-BC-CNFs electrodes exhibit excellent flexibility. To the best knowledge of the authors, this is the first report on flexible BC-CNF/metal oxide hybrid electrodes despite the great advancements in the development of metal oxide loaded CNFs.²⁹

Herein, we report the preparation of Fe₃O₄-BC-CNFs anodes for LIBs via the hydrothermal method using an aqueous solution followed by carbonization. The effect of the concentration of iron source material on the morphology, structure, and electrochemical performance of the Fe₃O₄-BC-CNFs electrodes was investigated. Our results demonstrate that the as-prepared Fe₃O₄-BC-CNFs maintain the 3D network structure of pristine BC aerogels and can endure repeated bending without structural failure. Using these 3D flexible materials, we assembled binder-free coin-type cells directly using the Fe₃O₄-BC-CNFs as the working electrodes that show extremely improved electrochemical performance over bare BC-CNFs and Fe₃O₄ nanoparticles. Furthermore, besides the excellent flexibility, the reversible capacity of the binder-free electrodes (754 mAh g⁻¹ at 100 mA g⁻¹ after 100 cycles) also outperforms

most of Fe₃O₄-carbon hybrids. The approach reported here is controllable, scalable, cost-effective, eco-friendly, and extendable to the preparation of other relevant BC-CNFs based flexible electrodes.

The general fabrication process and formation mechanism of Fe₃O₄-BC-CNFs are illustrated in Fig. 1a (the detailed experiments and sample designation are presented in the ESI). In a typical procedure, a BC aerogel was firstly immersed in an aqueous solution of Fe(NO₃)₃•9H₂O for 48 h at room temperature to allow the adsorption of Fe ions to the surface of BC nanofibers via chemiadsorption and electro adsorption. The -OH groups on BC nanofibers act as active sites for the adsorption of Fe ions. Thus, the intrinsic uniform distribution of -OH groups on BC nanofibers can ensure the even dispersion of Fe ions on BC nanofibers and subsequent uniform distribution of Fe₃O₄ nanoparticles on BC-CNFs. The resulting sample was immersed in the urea aqueous solution under agitation, and subsequently transferred to a closed container to allow the hydrothermal reactions ((1) CO(NH₂)₂ + 3H₂O → CO₂ + 2NH₄OH; (2) Fe³⁺ + 3OH⁻ → Fe(OH)₃; (3) 2Fe(OH)₃ → Fe₂O₃+ 3H₂O), resulting in Fe₂O₃-BC. The Fe₂O₃-BC was carbonized in a tube furnace under nitrogen atmosphere, resulting in Fe₃O₄-BC-CNFs (C + 6Fe₂O₃ → 4Fe₃O₄ + CO₂). Obviously, both the hydrothermal process and carbonization can be easily scaled up. Furthermore, all raw materials and reagents involved are quite low-cost and not poisonous. During the hydrothermal process, the amount of Fe₂O₃ in the Fe₂O₃-BC aerogels (corresponding to the amount of Fe₃O₄ in the Fe₃O₄-BC-CNFs) can be easily controlled by tuning the concentration of Fe(NO₃)₃•9H₂O.

The morphology and structure of Fe₃O₄-BC-CNFs were characterized by SEM, TEM, XRD, XPS, FTIR, and Raman analyses. As shown in Fig. 1b-d, after decorating with Fe₂O₃ (the crystalline structure of the deposits is α -Fe₂O₃ as confirmed by XRD result shown in Fig. S1), all Fe₂O₃-BCs inherit the intrinsic 3D porous network structure of pristine BC aerogels (in line with our previous report³⁰) regardless of the Fe₂O₃ loading. Moreover, we find that the Fe₂O₃ loading increases with the concentration of Fe(NO₃)₃•9H₂O in the aqueous solutions, which can be identified from the macroscopic color change of the samples (shown in Fig. 1b-d as insets). This indicates that the Fe₂O₃ loading on BC is controllable. Fig. 1e-g demonstrates that the as-prepared Fe₃O₄-BC-CNFs (the deposits on BC-CNFs are identified to be Fe₃O₄ as shown in Fig. S2, showing a complete transformation from Fe₂O₃ to Fe₃O₄) still retain the intrinsic 3D porous network structure of pristine BC aerogels. TEM images (Fig. 1h, j, and l) reveal nanoparticle aggregation only in Fe₃O₄-BC-CNFs-20 (red frame in Fig. 1l) due to its high Fe₃O₄ loading. The increased amount of Fe₃O₄ nanoparticles on BC-CNFs with increasing Fe(NO₃)₃•9H₂O concentration can be evidenced by HRTEM images (Fig. 1i, k, and m). TGA analysis (Fig. S7) further confirms the highest Fe₃O₄ content in Fe₃O₄-BC-CNFs-20, which is 58.3 wt%, while the Fe₃O₄ contents for Fe₃O₄-BC-CNFs-05 and Fe₃O₄-BC-CNFs-10 are 34.1 and 47.1 wt%, respectively. However, particle size measurement (Fig. S3) reveals that there is no significant difference in the diameter of Fe₃O₄ nanoparticles among Fe₃O₄-BC-CNFs-05, Fe₃O₄-BC-CNFs-10, and Fe₃O₄-BC-CNFs-20 ($p > 0.05$), suggesting that Fe(NO₃)₃•9H₂O concentration does not affect the size of Fe₃O₄

nanoparticles. This indicates that neither particle size nor crystalline structure is affected by the $\text{Fe}(\text{NO}_3)_3 \cdot 9\text{H}_2\text{O}$ concentration as confirmed by XRD results (Fig. S2) and interplanar spacing values (Fig. S4). In conjunction with XRD results, EDX (energy-dispersive X-ray spectroscopy) (Fig. S5) and XPS wide scan spectrum (Fig. S6a) results confirm the high purity of the as-prepared Fe_3O_4 (Cu signal is from the copper mesh for TEM sample preparation). As expected, the peaks located at 710.9 and 724.3 eV (Fig. S6b) correspond to Fe 2p_{3/2} and Fe 2p_{1/2}, respectively,³¹ and the satellite peak that is characteristic for $\gamma\text{-Fe}_2\text{O}_3$ is not detected, excluding the presence of $\gamma\text{-Fe}_2\text{O}_3$ in the sample.³² This finding confirms that the oxide in the sample is only Fe_3O_4 , consistent with XRD results shown in Fig. S2. The spectrum in Fig. S6c indicates that there are oxygenated functional groups on BC-CNFs, which may support their good hydrophilicity.³³ In order to determine the carbon structure of $\text{Fe}_3\text{O}_4\text{-BC-CNFs}$, Raman analysis was conducted (Fig. S8). The Raman spectrum of the pristine BC-CNFs shows a D-band at 1342 cm^{-1} and a G-band at 1590 cm^{-1} . The D-band is attributed to defects and disordered portions of carbon (sp^3 -coordinated) whereas the G-band is indicative of ordered graphitic crystallites of carbon (sp^2 -coordinated).^{22, 34} Therefore, the intensity ratio (R) of D band to G band, $R = I_D/I_G$ is an indication of the relative amount of carbon defects.³⁵ As shown in Fig. S8 and Table S1, both G-band and D band show negative shifts, likely due to the interactions between the two components as aforementioned, which might change the Raman peak frequency.³⁶ Furthermore, the R values of $\text{Fe}_3\text{O}_4\text{-BC-CNFs}$ are larger than that of BC-CNFs and they increase with the $\text{Fe}(\text{NO}_3)_3 \cdot 9\text{H}_2\text{O}$ concentration

(Table S1). The increased R values of $\text{Fe}_3\text{O}_4\text{-BC-CNFs}$ further indicate the interactions between CNFs and iron oxides during carbonization, which increase the amount of defects and disordered portions of carbon on the surface of CNFs. Nitrogen isothermal adsorption/desorption measurement and pore size distribution analysis were performed (Fig. S9). Fig. S9a shows a typical type IV isotherm. The pore size distribution (Fig. S9b) reveals the large quantity of mesopores, which allow fast diffusion of electrolyte ions owing to the reduced solid-state transport length.³⁷ The Brunauer-Emmett-Teller specific surface area was calculated to be $322 \text{ m}^2 \text{ g}^{-1}$, which is higher than that of BC-CNF-network-coated MnO_2 ³⁷ and 3D graphene foams cross-linked with encapsulated Fe_3O_4 nanospheres.³⁸ These results suggest that $\text{Fe}_3\text{O}_4\text{-BC-CNFs-10}$ displays a highly porous structure with a large number of mesopores and large specific surface area, which are favorable for electrolyte accessibility and rapid lithium-ion diffusion.³⁸

Prior to electrochemical measurements, we tested the flexibility of a representative sample ($\text{Fe}_3\text{O}_4\text{-BC-CNFs-10}$) by repeated bending and compressing. We find that the $\text{Fe}_3\text{O}_4\text{-BC-CNFs-10}$ shows superior flexibility and structural stability. After many cycles of bending and compressing, the sample can recover to its original shape without breaking (Fig. 2), suggesting that this material is foldable and mechanically stable,³⁹ which will make it an attractive candidate for further applications in flexible LIBs.^{2, 40, 41} To further confirm its flexibility, we measured its electrical conductivity before and after bending tests according to previous reports.³⁹

⁴² We do not find any significant difference in the electrical conductivity before ($2.0 \pm$

0.2 S m⁻¹) and after (2.1 ± 0.1 S m⁻¹) bending tests ($p > 0.05$), further suggesting the excellent flexibility of the material.

The CV profiles for the initial three cycles of the representative sample (Fe₃O₄-BC-CNFs-10) were measured. As shown in Fig. S10, there are two reduction peaks at 0.61 and 0.79 V (vs Li⁺/Li) only in the first cycle, which is similar to previous reports.^{43, 44} In the subsequent cycles, the reduction peak at 0.61 V (vs Li⁺/Li) disappears, indicating that this peak corresponds to some irreversible processes (such as the inevitable formation of a stable solid electrolyte interface (SEI) layer and the electrolyte decomposition in the first cycle.²² The 0.79 V (vs Li⁺/Li) peak is usually ascribed to the reversible conversion of Fe₃O₄ to Fe and the formation of amorphous Li₂O (Fe₃O₄ + 8Li⁺ + 8e⁻ → 3Fe + 4Li₂O).⁴⁵⁻⁴⁸ The broad oxidation peak at around 1.67 V (vs Li⁺/Li) is ascribed to the reversible oxidization of Fe⁰ to Fe²⁺/Fe³⁺.^{45, 46, 49} In the second and third cycles, the oxidation peak is positively shifted to 1.70 and 1.94 V (vs Li⁺/Li), respectively, likely due to the polarization of the active Fe₃O₄ in the first cycle.^{45, 49}

The discharge and charge voltage profiles of Fe₃O₄-BC-CNFs-10 shown in Fig. 3a are in good agreement with the CV measurements. Two plateaus at about 0.8 and 1.0 V (vs. Li⁺/Li) can be observed only in the first discharge voltage profile, corresponding to the peaks in CV curves. The difference in the discharge voltage plateau in the first cycle and subsequent cycles indicates that the irreversible reactions occurred in the first cycle, which agrees well with the CV results that the peak location and intensity in the first scan are different from those in the subsequent scans.

As shown in Fig. 3b, no obvious discharge plateau can be seen for bare BC-CNFs while an obvious discharge plateau at around 1.0 V (vs. Li⁺/Li) is detected for bare Fe₃O₄ nanoparticles (Fig. S11), which is consistent with previous reports (0.75–1.0 V vs. Li⁺/Li for bare iron oxide anodes⁵⁰). As shown in Fig. 3, Fe₃O₄-BC-CNFs and bare BC-CNFs show obvious irreversible discharge capacities (irreversible portions of the capacity during the first discharge–charge process range from 43 to 57%) in the first cycle, which are close to previously reported values for BC-CNFs,²⁵ Fe₃O₄-C,^{50, 51} and Fe₂O₃-CNF.²⁴ The irreversible capacities in the first cycle are usually ascribed to the inevitable formation of SEI and decomposition of electrolytes.^{48, 52} Furthermore, we notice that the capacities in the first cycle are larger than the theoretical capacities of Fe₃O₄-BC-CNFs and bare BC-CNFs, which is common to anode materials.^{38, 53-56} The extra capacities can be ascribed to the formation of SEI layer, further lithium consumption via interfacial reactions, the conversion of Fe₃O₄ to Fe nanoparticles, and trapped Li⁺ in the pores.^{36, 43, 48}

The cycling performance and Coulombic efficiency were also measured (Fig. 4 and Fig. S12). After 100 cycles under a current density of 100 mA g⁻¹, bare BC-CNFs (Fig. 4a) and Fe₃O₄ nanoparticles (Fig. S11) exhibit reversible capacities of ca. 297 and 200 mAh g⁻¹, respectively. Note that Fe₃O₄-BC-CNFs (Fig. 4b-d) demonstrate much higher reversible capacities, which are 540, 754, and 501 mAh g⁻¹ for Fe₃O₄-BC-CNFs-05, Fe₃O₄-BC-CNFs-10, and Fe₃O₄-BC-CNFs-20, respectively, indicating that the Fe₃O₄-BC-CNFs-10 with a moderate Fe₃O₄ content exhibits the best cycling performance. The significantly improved cycling performance of

Fe₃O₄-BC-CNFs over bare BC-CNFs and Fe₃O₄ suggests that there are synergistic effects between the two components. On the one hand, Fe₃O₄ nanoparticles are the dominant active component. On the other hand, BC-CNFs acting as a scaffold, not only support the uniform distribution of Fe₃O₄ nanoparticles and prevent the neighboring nanoparticles from fusion in the cycling process, but also provide numerous voids which favor the fast diffusion and transport of lithium ions.²⁵ Therefore, the best cycling performance of Fe₃O₄-BC-CNFs-10 can be elucidated. Compared with Fe₃O₄-BC-CNFs-10, the poorer performance of Fe₃O₄-BC-CNFs-05 is due to the less amount of active Fe₃O₄ nanoparticles and the inferior behavior of Fe₃O₄-BC-CNFs-20 is related to the excess and aggregated Fe₃O₄ nanoparticles. It should be pointed out that the reversible capacity (754 mAh g⁻¹) of Fe₃O₄-BC-CNFs-10 is higher than most of the previously reported relevant electrodes such as SnO₂-decorated BC-CNFs (600 mAh g⁻¹),²⁵ Fe₃O₄/CNTs (656 mAh g⁻¹),⁵⁷ electrospun Fe₃O₄/C microbelts (710 mAh g⁻¹),⁴⁶ Fe₃O₄/C nanofibers (508 mAh g⁻¹),⁵⁸ Fe₃O₄/C composites (610 mAh g⁻¹),⁵⁰ and graphene-encapsulated Fe₃O₄ (650 mAh g⁻¹).⁴⁵ The excellent cycling performance of Fe₃O₄-BC-CNFs-10 is attributed to the 3D porous network structure. First, the distinct 3D network structure and large surface area of Fe₃O₄-BC-CNFs is believed to be an important factor for the enhanced electrochemical performance¹⁵ since 3D structure can enhance the transport of ion and electron and the large surface area can further facilitate fast Li ion insertion/extraction.⁵⁹ Second, the carbon scaffold with 3D interconnectivity and high electronic conductivity acts as efficient conductive path and thus is of benefit to fast

electron conduction. Third, the numerous interconnected pores not only provide enough space for the volume expansion and contraction, thus relieving the impact of volume change of active materials and avoiding the pulverization of the electrode,⁴⁶ but also favors fast transport of Li ions.

The rate performance of Fe₃O₄-BC-CNFs-10 was compared with bare BC-CNFs and Fe₃O₄ (Fig. 5a-c). The specific discharge capacities of BC-CNFs and Fe₃O₄ decrease to 157 and 156 mAh g⁻¹, respectively, at 1000 mA g⁻¹ while Fe₃O₄-BC-CNFs-10 delivers a much higher discharge capacity of 410 mAh g⁻¹, revealing excellent rate performance. Furthermore, its capacity can be completely recovered when the current density is turned back to 100 mA g⁻¹ after cycling at various currents from 100 to 1000 mA g⁻¹. This finding further confirms the excellent rate performance of Fe₃O₄-BC-CNFs-10.

The electrochemical impedance spectroscopy (EIS) was used to determine the charge transport kinetics of the Fe₃O₄-BC-CNFs-10 electrode. Fig. 5d shows the Nyquist plots of Fe₃O₄-BC-CNFs-10 and bare Fe₃O₄ anodes. The Nyquist plots exhibit typical two distinct parts including a semicircle in the middle frequency range and an oblique straight line in the low frequency range. The plots were fitted with the equivalent circuit model as depicted in the inset in Fig. 5d and the fitting values of some significant kinetic parameters are listed in Table S2. R_f is the resistance for lithium ion migration through the SEI film, R_{ct} represents charge-transfer impedance at electrode–electrolyte interface, and the Warburg impedance (Z_w) is related to lithium ions transfer process.⁶⁰ The resistance for lithium ion migration (R_f) through

SEI film of Fe₃O₄-BC-CNFs-10 (23.0 Ω) is smaller than that of bare Fe₃O₄ (39.8 Ω), implying that a stable SEI film is formed for Fe₃O₄-BC-CNFs-10. It is reported that the cell impedance is mainly determined by R_{ct} .⁶¹ Note that the R_{ct} of Fe₃O₄-BC-CNFs-10 (136.2 Ω) is much smaller than that (361.9 Ω) of bare Fe₃O₄ nanoparticles, which can lead to rapid electron transport during the electrochemical lithium insertion/extraction reaction. The lower R_{ct} contributes to the superior electrochemical performance of Fe₃O₄-BC-CNFs-10. This finding is in agreement with common notions that one of the most widely used approaches to improve the electrochemical performance of the metal oxide electrodes is to fabricate composites with carbonaceous materials such that the conductivity is improved and the volume change of the active metal oxides is buffered.^{37, 62, 63} As shown in Table S2, the decreased R_f and R_{ct} values after cycling are likely due to the formation of a good conductive pathway in the electrodes⁶⁴ and generally imply the electrode possesses a high electrical conductivity and a rapid charge-transfer reaction for lithium ion insertion and extraction.⁶⁵

Although its rate capability and cycling performance are not as good as some Fe₃O₄-graphene hybrids,^{34, 38, 66-68} the superior performance over BC-CNFs, bare Fe₃O₄ nanoparticles, and most Fe₃O₄-carbon hybrids demonstrates that the effectiveness of the strategy of immobilizing active materials onto 3D BC-CNFs. More importantly, the excellent flexibility, binder-free nature, cost-effectiveness, and mass-production potential make this anode material very competitive and attractive in high performance flexible power sources.

In summary, highly dispersed Fe_3O_4 nanoparticles with an average size of about 10 nm have been successfully loaded on the surface of 3D BC-CNFs through scalable, cost-effective, and eco-friendly hydrothermal method followed by carbonization. The hydrothermal method is able to control the amount of Fe_2O_3 nanoparticles and their distribution on the surface of BC nanofibers. The subsequent carbonization simultaneously converts Fe_2O_3 and BC nanofibers to Fe_3O_4 and CNFs, respectively, resulting in BC- Fe_3O_4 -CNFs. The as-prepared BC- Fe_3O_4 -CNFs-10 with an appropriate Fe_3O_4 loading sustains the 3D porous network structure of pristine BC and exhibits excellent flexibility and mechanical stability. The flexible and binder-free electrode built of BC- Fe_3O_4 -CNFs-10 exhibits high reversible capacity and excellent rate performance. The excellent electrochemical performance is attributed to its unique structure. The uniform distribution of Fe_3O_4 nanoparticles enhances the utilization of active component and the interconnected CNFs structure imparts the electrode with good conductivity and facilitates the transport for both electrons and Li ions. The large quantity of pores can absorb electrolytes and buffer the volume changes during charge-discharge cycling. The strategy presented here is a general, low-cost, safe, and broadly applicable method, providing new avenues for the engineering of flexible BC-CNF based electrodes with enhanced performance.

Acknowledgements

This work is supported by the National Natural Science Foundation of China (Grant No. 51172158).

Notes and references

1. M. Wakihara, *Mater. Sci. Engin.: R: Reports*, 2001, **33**, 109-134.
2. N. Li, Z. Chen, W. Ren, F. Li and H.-M. Cheng, *Proc. Natl Acad. Sci.*, 2012, **109**, 17360-17365.
3. H. Kim, X. Huang, X. Guo, Z. Wen, S. Cui and J. Chen, *ACS Appl. Mater. Interfaces*, 2014, **6**, 18590-18596.
4. M. D. Lima, S. Fang, X. Lepró, C. Lewis, R. Ovalle-Robles, J. Carretero-González, E. Castillo-Martínez, M. E. Kozlov, J. Oh and N. Rawat, *Science*, 2011, **331**, 51-55.
5. X. Xu, G. Wang and H. Wang, *Chem. Engin. J.*, 2015, **266**, 222-232.
6. D. Wei, M. R. Astley, N. Harris, R. White, T. Ryhänen and J. Kivioja, *Nanoscale*, 2014, **6**, 9536-9540.
7. M. Inagaki, Y. Yang and F. Kang, *Adv. Mater.*, 2012, **24**, 2547-2566.
8. Z.-Y. Wu, C. Li, H.-W. Liang, Y.-N. Zhang, X. Wang, J.-F. Chen and S.-H. Yu, *Sci. Rep.*, 2014, **4**, 4079.
9. X. Shen, D. Mu, S. Chen, B. Xu, B. Wu and F. Wu, *J. Alloys Compd.*, 2013, **552**, 60-64.
10. Y. Wan, G. Zuo, F. Yu, Y. Huang, K. Ren and H. Luo, *Sur. Coat. Technol.*, 2011, **205**, 2938-2946.
11. Z. Yin, C. Lee, S. Cho, J. Yoo, Y. Piao and Y. S. Kim, *Small*, 2014, **10**, 5047-5052.
12. W. J. Hyun, O. O. Park and B. D. Chin, *Adv. Mater.*, 2013, **25**, 4729-4734.
13. D. Zhang, K. Ryu, X. Liu, E. Polikarpov, J. Ly, M. E. Tompson and C. Zhou,

- Nano Lett.*, 2006, **6**, 1880-1886.
14. H.-W. Liang, Q.-F. Guan, L.-T. S. Zhu-Zhu, H.-B. Yao, X. Lei and S.-H. Yu, *NPG Asia Mater.*, 2012, **4**, e19.
15. L. Wang, C. Schütz, G. Salazar-Alvarez and M.-M. Titirici, *RSC Adv.*, 2014, **4**, 17549-17554.
16. C. Kim, K. S. Yang, M. Kojima, K. Yoshida, Y. J. Kim, Y. A. Kim and M. Endo, *Adv. Funct. Mater.*, 2006, **16**, 2393-2397.
17. D. Nan, Z.-H. Huang, R. Lv, L. Yang, J.-G. Wang, W. Shen, Y. Lin, X. Yu, L. Ye, H. Sun and F. Kang, *J. Mater. Chem. A*, 2014, **2**, 19678-19684.
18. J. Jin, Z.-q. Shi and C.-y. Wang, *Electrochim. Acta*, 2014, **141**, 302-310.
19. J. Jin, S.-j. Yu, Z.-q. Shi, C.-y. Wang and C.-b. Chong, *J. Power Sources*, 2014, **272**, 800-807.
20. Y. Wu, M. V. Reddy, B. V. R. Chowdari and S. Ramakrishna, *ACS Appl. Mater. Interfaces*, 2013, **5**, 12175-12184.
21. C. A. Bonino, L. Ji, Z. Lin, O. Toprakci, X. Zhang and S. A. Khan, *ACS Appl. Mater. Interfaces*, 2011, **3**, 2534-2542.
22. L. Ji, O. Toprakci, M. Alcoutlabi, Y. Yao, Y. Li, S. Zhang, B. Guo, Z. Lin and X. Zhang, *ACS Appl. Mater. Interfaces*, 2012, **4**, 2672-2679.
23. L. Wang, Y. Yu, P. Chen, D. Zhang and C. Chen, *J. Power Sources*, 2008, **183**, 717-723.
24. Y. Wu, P. Zhu, M. V. Reddy, B. V. R. Chowdari and S. Ramakrishna, *ACS Appl. Mater. Interfaces*, 2014, **6**, 1951-1958.

25. B. Wang, X. Li, B. Luo, J. Yang, X. Wang, Q. Song, S. Chen and L. Zhi, *Small*, 2013, **9**, 2399-2404.
26. H.-W. Liang, Z.-Y. Wu, L.-F. Chen, C. Li and S.-H. Yu, *Nano Energy*, 2015, **11**, 366-376.
27. Z. Wang, D. Luan, S. Madhavi, Y. Hu and X. W. Lou, *Energy Environ. Sci.*, 2012, **5**, 5252-5256.
28. L. Zhang, H. B. Wu and X. W. D. Lou, *Adv. Energy Mater.*, 2014, **4**, 1300958.
29. S. Liu, Z. Wang, C. Yu, H. B. Wu, G. Wang, Q. Dong, J. Qiu and A. Eychmüller, *Adv. Mater.*, 2013, **25**, 3462-3467.
30. H. Si, H. Luo, G. Xiong, Z. Yang, S. R. Raman, R. Guo and Y. Wan, *Macromol. Rapid Commun.*, 2014, **35**, 1706-1711.
31. Y. Zhan, F. Meng, X. Yang, R. Zhao and X. Liu, *Materials Science and Engineering B-Advanced Functional Solid-State Materials*, 2011, **176**, 1333-1339.
32. M. Zong, Y. Huang, Y. Zhao, X. Sun, C. Qu, D. Luo and J. Zheng, *RSC Advances*, 2013, **3**, 23638.
33. Y. Liu, T. Lu, Z. Sun, D. H. Chua and L. Pan, *J. Mater. Chem. A*, 2015, **3**, 8693-8700.
34. L. G. Cançado, M. A. Pimenta, B. R. A. Neves, M. S. S. Dantas and A. Jorio, *Phys. Rev. Lett.*, 2004, **93**, 247401.
35. Z. Niu, J. Chen, H. H. Hng, J. Ma and X. Chen, *Adv. Mater.*, 2012, **24**, 4144-4150.

36. Z. Ni, Y. Wang, T. Yu and Z. Shen, *Nano Res.*, 2008, **1**, 273-291.
37. L. F. Chen, Z. H. Huang, H. W. Liang, Q. F. Guan and S. H. Yu, *Adv. Mater.*, 2013, **25**, 4746-4752.
38. W. Wei, S. Yang, H. Zhou, I. Lieberwirth, X. Feng and K. Müllen, *Adv. Mater.*, 2013, **25**, 2909-2914.
39. L. Jabbour, C. Gerbaldi, D. Chaussy, E. Zeno, S. Bodoardo and D. Beneventi, *J. Mater. Chem.*, 2010, **20**, 7344-7347.
40. S. Leijonmarck, A. Cornell, G. Lindbergh and L. Wågberg, *J. Mater. Chem. A*, 2013, **1**, 4671-4677.
41. H. Nishide and K. Oyaizu, *Science*, 2008, **319**, 737-738.
42. J. Chen, H. Bi, S. Sun, Y. Tang, W. Zhao, T. Lin, D. Wan, F. Huang, X. Zhou and X. Xie, *ACS Appl. Mater. Interfaces*, 2013, **5**, 1408-1413.
43. C. He, S. Wu, N. Zhao, C. Shi, E. Liu and J. Li, *ACS Nano*, 2013, **7**, 4459-4469.
44. N. Yan, F. Wang, H. Zhong, Y. Li, Y. Wang, L. Hu and Q. Chen, *Sci. Rep.*, 2013, **3**, 1568.
45. J. Z. Wang, C. Zhong, D. Wexler, N. H. Idris, Z. X. Wang, L. Q. Chen and H. K. Liu, *Chemistry*, 2011, **17**, 661-667.
46. L. Lang and Z. Xu, *ACS Appl. Mater. Interfaces*, 2013, **5**, 1698-1703.
47. Z. Xiao, Y. Xia, Z. Ren, Z. Liu, G. Xu, C. Chao, X. Li, G. Shen and G. Han, *J. Mater. Chem.*, 2012, **22**, 20566-20573.
48. T. Yoon, C. Chae, Y.-K. Sun, X. Zhao, H. H. Kung and J. K. Lee, *J. Mater.*

- Chem.*, 2011, **21**, 17325-17330.
49. D. Li, X. Li, S. Wang, Y. Zheng, L. Qiao and D. He, *ACS Appl. Mater. Interfaces*, 2013, **6**, 648-654.
50. G. Chen, M. Zhou, J. Catanach, T. Liaw, L. Fei, S. Deng and H. Luo, *Nano Energy*, 2014, **8**, 126-132.
51. D.-Y. Park and S.-T. Myung, *ACS Appl. Mater. Interfaces*, 2014, **6**, 11749-11757.
52. C. Liu, F. Li, L. P. Ma and H. M. Cheng, *Adv. Mater.*, 2010, **22**, E28-E62.
53. B. Li, H. Cao, J. Shao and M. Qu, *Chem. Commun.*, 2011, **47**, 10374-10376.
54. Y. Yu, Y. Zhu, H. Gong, Y. Ma, X. Zhang, N. Li and Y. Qian, *Electrochim. Acta*, 2012, **83**, 53-58.
55. X. Fan, J. Shao, X. Xiao, L. Chen, X. Wang, S. Li and H. Ge, *J. Mater. Chem. A*, 2014, **2**, 14641-14648.
56. G. Zhou, D.-W. Wang, F. Li, L. Zhang, N. Li, Z.-S. Wu, L. Wen, G. Q. Lu and H.-M. Cheng, *Chem. Mater.*, 2010, **22**, 5306-5313.
57. Y. He, L. Huang, J.-S. Cai, X.-M. Zheng and S.-G. Sun, *Electrochim. Acta*, 2010, **55**, 1140-1144.
58. S. Gu, Y. Liu, G. Zhang, W. Shi, Y. Liu and J. Zhu, *RSC Adv.*, 2014, **4**, 41179-41184.
59. M. Tian, W. Wang, Y. Liu, K. L. Jungjohann, C. T. Harris, Y.-C. Lee and R. Yang, *Nano Energy*, 2015, **11**, 500-509.
60. H. Tao, L.-Z. Fan, W.-L. Song, M. Wu, X. He and X. Qu, *Nanoscale*, 2014, **6**,

- 3138-3142.
61. C. Chen, J. Liu and K. Amine, *J. Power Sources*, 2001, **96**, 321-328.
62. X. Zhu, Y. Zhu, S. Murali, M. D. Stoller and R. S. Ruoff, *ACS Nano*, 2011, **5**, 3333-3338.
63. S. Li, W. Xie, S. Wang, X. Jiang, S. Peng and D. He, *J. Mater. Chem. A*, 2014, **2**, 17139-17145.
64. G. Gu, J. Cheng, X. Li, W. Ni, Q. Guan, G. Qu and B. Wang, *J. Mater. Chem. A*, 2015, **3**, 6642-6648.
65. Z.-J. Fan, J. Yan, T. Wei, G.-Q. Ning, L.-J. Zhi, J.-C. Liu, D.-X. Cao, G.-L. Wang and F. Wei, *ACS Nano*, 2011, **5**, 2787-2794.
66. C. Liang, T. Zhai, W. Wang, J. Chen, W. Zhao, X. Lu and Y. Tong, *J. Mater. Chem. A*, 2014, **2**, 7214-7220.
67. L. Jing, A. Fu, H. Li, J. Liu, P. Guo, Y. Wang and X. S. Zhao, *RSC Adv.*, 2014, **4**, 59981-59989.
68. S. Liu, Y. Dong, C. Zhao, Z. Zhao, C. Yu, Z. Wang and J. Qiu, *Nano Energy*, 2015, **12**, 578-587.

Figure captions

Fig. 1 The preparation process of Fe₃O₄-BC-CNFs (a), SEM images of Fe₂O₃-BC-05 (b), Fe₂O₃-BC-10 (c), Fe₂O₃-BC-20 (d), Fe₃O₄-BC-CNFs-05 (e), Fe₃O₄-BC-CNFs-10 (f), and Fe₃O₄-BC-CNFs-20 (g), TEM and HR-TEM images of Fe₃O₄-BC-CNFs-05 (h, i), Fe₃O₄-BC-CNFs-10 (j, k), and Fe₃O₄-BC-CNFs-20 (l, m) (insets in b-d showing corresponding macroscopic photos, red frame in l showing aggregated nanoparticles).

Fig. 2 Sequential photographs of the Fe₃O₄-BC-CNFs-10 during repeated bending and compressing demonstrating the excellent flexibility.

Fig. 3 Discharge/charge profiles of Fe₃O₄-BC-CNFs-10 (a), BC-CNFs (b), Fe₃O₄-BC-CNFs-05 (c), and Fe₃O₄-BC-CNFs-20 (d).

Fig. 4 Charge and discharge capacities with Coulombic efficiency as a function of cycle number of BC-CNFs (a), Fe₃O₄-BC-CNFs-10 (b), Fe₃O₄-BC-CNFs-05 (c), and Fe₃O₄-BC-CNFs-20 (d) at a current density 100 mA g⁻¹.

Fig 5 Rate performance of Fe₃O₄-BC-CNFs-10 (a), BC-CNFs (b), and bare Fe₃O₄ nanoparticles at various current densities(c), Nyquist plots of Fe₃O₄-BC-CNFs-10 (d1 and d3) and bare Fe₃O₄ (d2) before (d1 and d2) and after (d3) rate performance tests (d), the symbols stand for the experimental data and the corresponding lines are the fitted curves, the inset shows the corresponding equivalent circuit model.

Fig. 1

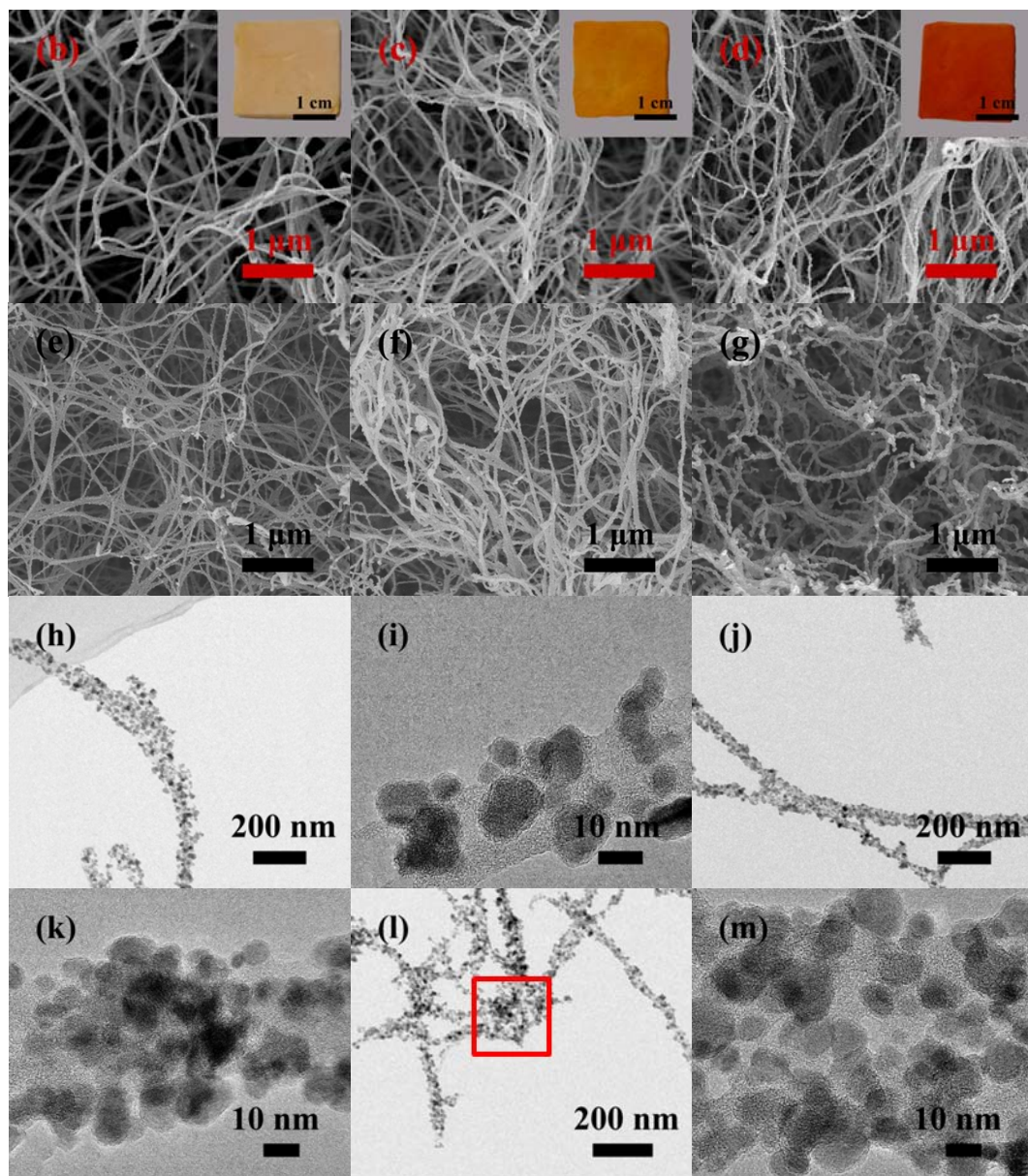
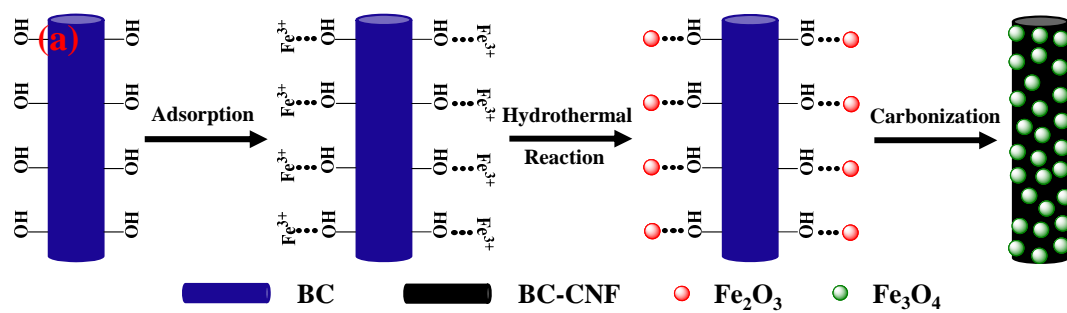


Fig. 2

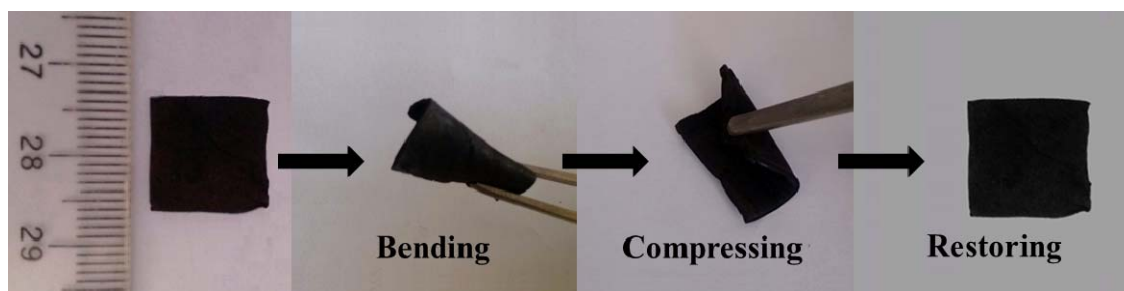


Fig. 3

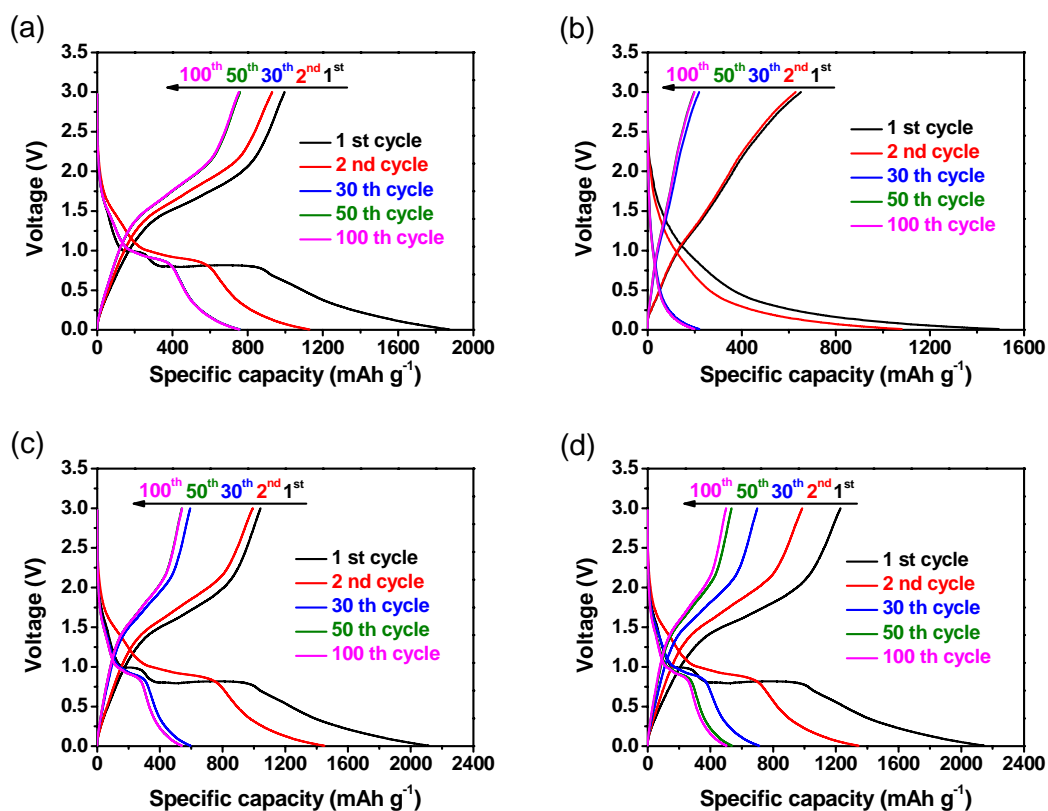


Fig. 4

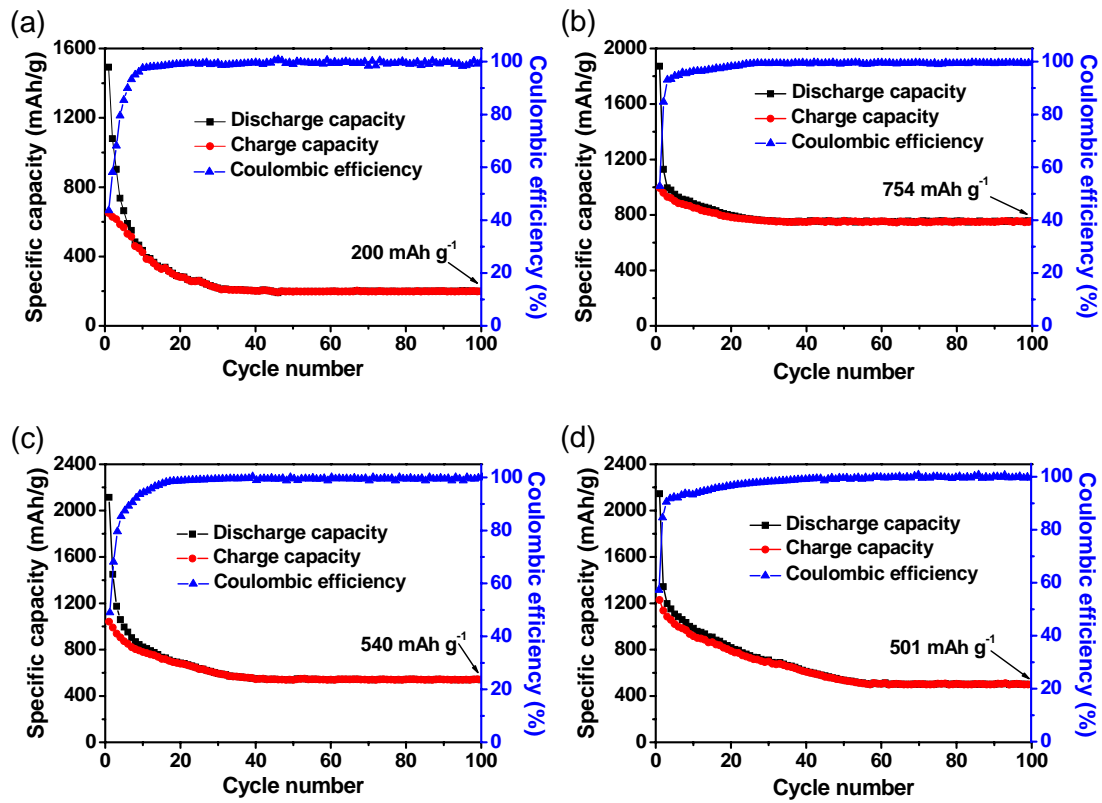
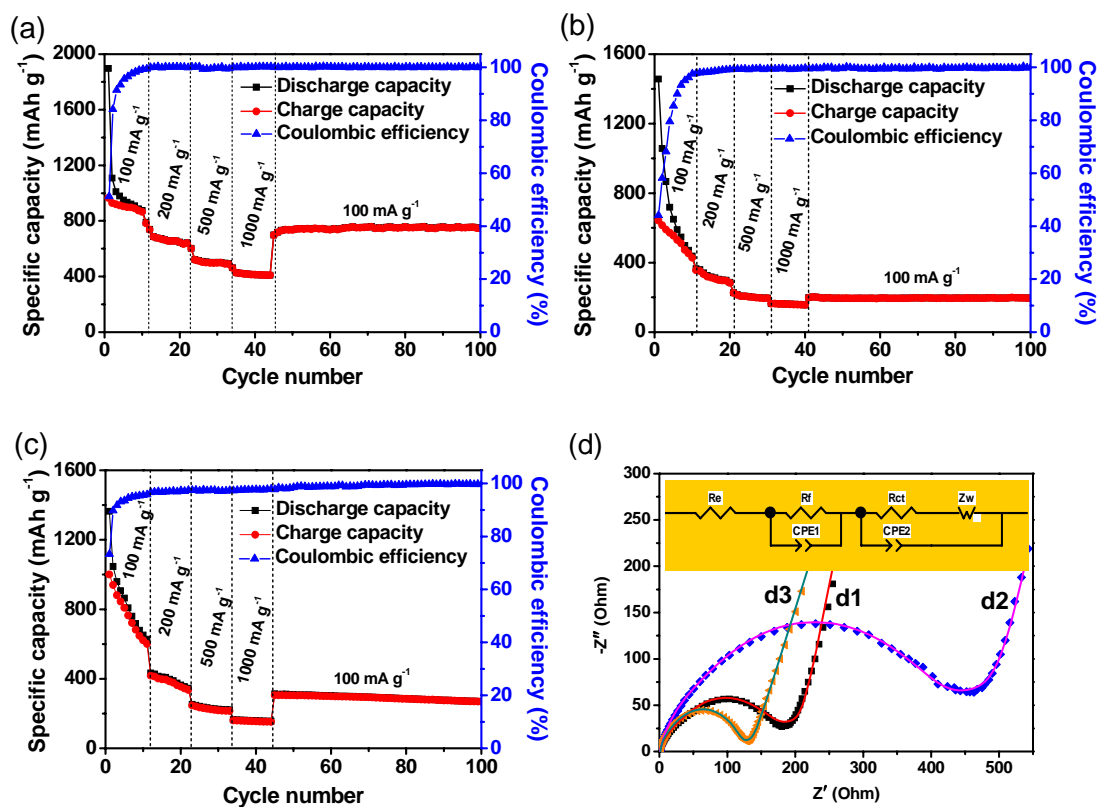


Fig. 5



A novel flexible nano- Fe_3O_4 -decorated three-dimensional carbon nanofiber aerogel derived from bacterial cellulose was fabricated via the hydrothermal approach followed by carbonization.

